

Deep Learning for Biospectroscopy and Biospectral Imaging: State-of-the-Art and Perspectives

With the advances in instrumentation and sampling techniques, there is an explosive growth of data from molecular and cellular samples. The call to extract more information from the large data sets has greatly challenged the conventional chemometrics method. Deep learning, which utilizes very large data sets for finding hidden features therein and for making accurate predictions for a wide range of applications, has been applied in an unbelievable pace in biospectroscopy and biospectral imaging in the recent 3 years. In this Feature, we first introduce the background and basic knowledge of deep learning. We then focus on the emerging applications of deep learning in the data preprocessing, feature detection, and modeling of the biological samples for spectral analysis and spectroscopic imaging. Finally, we highlight the challenges and limitations in deep learning and the outlook for future directions.

Hao He, Sen Yan, Danya Lyu, Mengxi Xu, Ruiqian Ye, Peng Zheng, Xinyu Lu, Lei Wang,* and Bin Ren*



Cite This: *Anal. Chem.* 2021, 93, 3653–3665

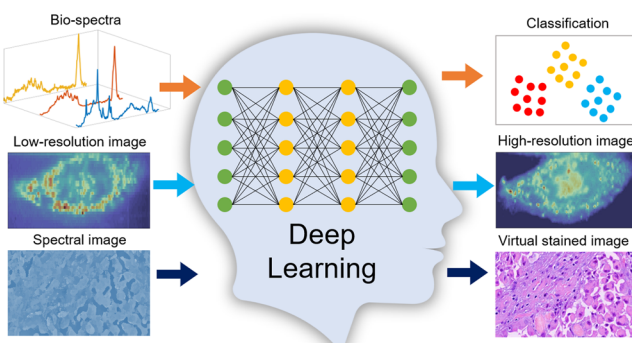


Read Online

ACCESS |

Metrics & More

Article Recommendations



Deep learning for biospectroscopy and bio-spectral imaging

Biospectroscopy and biospectral imaging is an increasing multidisciplinary field that utilizes the spectroscopic methods to investigate the biological systems at the molecular, cellular, and tissue levels. Among them, Raman spectroscopy,^{1,2} infrared spectroscopy (IR),^{3,4} fluorescence spectroscopy,^{5,6} etc. have been widely used in the biological and biomedical researches over the past decades. The inherent complexity of spectroscopic data from biosamples requires chemometrics methods to facilitate the wide application of these techniques. Due to their powerful data analysis ability such as interference removal, data reconstruction, and classification, chemometrics methods have been widely applied in the preprocessing, feature detection, and modeling.^{7–11} The raw data should be first preprocessed to improve its reliability and quality by removing interference such as background and noise or enhancing the spectral or spatial resolution. Then, the next step is to find the interested features as an abstract of the data. These features can be the principal components (PCs) or latent variables (LVs) of the spectra, region of interested

(ROI), or the morphological parameters of the target objects, etc., which can be used to decipher the contents of the data. The last step is to classify and regress by modeling. Modeling heavily relies of chemometrics methods, including linear discriminant analysis (LDA),^{12,13} logistic regression (LR),^{13,14} support vector machine (SVM),^{9,13,15} k-nearest neighbor (KNN),^{15–17} random forest (RF),^{13,18} and decision tree.^{13,19} These methods allow successful spectra and images analysis of complex biological samples such as cell identification,^{20–28} disease diagnosis,^{29–35} and forensic analysis.^{36–39}

However, the traditional chemometrics methods are increasingly challenged. On one hand, the high dimensionality of the biospectra or bioimages and the multivariate even megavariate nature, as a result of the inherent complexity of the biological systems,⁴⁰ increase the difficulty of data analysis. Particularly, the vibrational spectra of single cellular or microbial systems suffers from the low signal-to-noise ratio (SNR), which further increases the difficulty for the data analysis. On the other hand, recent advances in technologies provide tools for high-throughput chemical profiling of biological systems in a cost-efficient manner, leading to the significantly increased data sizes. This not only leads to the difficulty in calculations but also prevents extraction of a subtle variation of sophisticated hidden features within the big data

Published: February 18, 2021



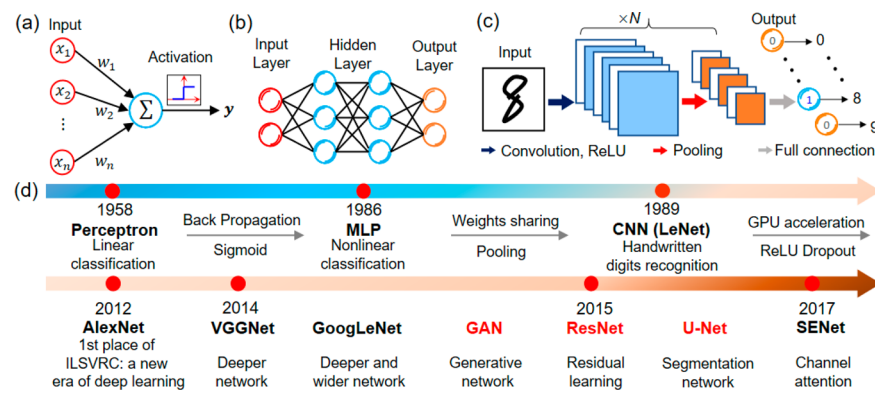


Figure 1. (a) Perceptron, (b) MLP, and (c) CNN. (d) The evolution of deep learning: from perceptron to CNN and the development of CNN in recent years.

through a single traditional data processing algorithm.^{41,42} Last but not least, the step-by-step procedure of the traditional data processing routine highly depends on the human experts' interferences, which is unfriendly for those who are not familiar with chemometrics. These factors have been the bottlenecks of the traditional chemometrics to some degree.

Deep learning, a branch of the machine learning which is known as the data-driven technique, has the potential to circumvent the above limitations. Specifically, here we focus on the deep convolutional neural networks (CNN), which are one of the most popular basic deep learning architectures and have been widely used. The supervised deep learning technique has attracted huge attention and enthusiasm in many fields such as the physical,^{43,44} chemical,^{45–47} and biomedical^{48–50} sciences, since the tremendous success of AlexNet on the ImageNet large scale visual recognition competition (ILSVRC).⁵¹ Basically, the dominating merits of deep learning can be attributed to three aspects. First, the multilevel feature extraction ability that is benefited from the layer-by-layer deep architecture⁵² enables it to perfectly extract the most valuable information relevant to the target problems. This allows deep learning to outperform most of the traditional algorithms and even the human experts in image classification, semantic segmentation, etc. Second, the data-driven nature of deep learning happens to meet the need to process the expanding big data. Concurrently, the high flexibility of the deep learning architecture enables the handling of different types of data, say, sequential data, an image, or a data cube.⁵³ Third, the deep learning models leverage the input and output in an end-to-end manner, thus can circumvent the trivial step-by-step procedure and decrease the human interferences once the model is well trained. These characteristics make deep learning a very powerful tool in biospectroscopy and biospectral imaging. With the advance of computing power of the graphics processing unit (GPU) and the increasing amount of available data, it is foreseeable that deep learning will make for greater successes in the near future. Several reviews^{54,55} have been published addressing both the classical machine learning and deep learning⁵⁶ technique for spectroscopic applications. However, a systematical introduction for the recently booming deep learning assisted spectroscopic analysis and its application is still urgently needed. This Feature serves as a practical tutorial by providing the principle first, followed by analyzing the recent applications of deep learning in biospectroscopy and imaging.

BRIEF OVERVIEW OF DEEP LEARNING

Evolution of Deep Learning. Deep learning is a subset of machine learning, including deep CNN, recurrent neural networks (RNN), and deep belief networks (DBN). Among them, RNNs⁵⁷ and DBNs⁵⁸ are widely used deep learning techniques in natural language processing and have achieved unprecedented success, such as speech recognition and machine translation. Deep CNNs, on the other hand, have revolutionized the data processing in many domains of science, especially in the visual related tasks. The origin of deep neural networks can be dated back to the perceptron that was reported by Rosenblatt et al.⁵⁹ in 1958. The architecture of perceptron is shown in Figure 1a. In perceptron, each input (x_1, \dots, x_n) is multiplied by a weight (w_1, \dots, w_n), which is summed together to generate the output with a step function. It learns through labeled data and can recognize simple patterns. In 1969,⁶⁰ it has been proven as a linear model that even cannot solve the basic exclusive OR problem. Since then neural networks enter a winter phase. Until 1986, Hinton et al.⁶¹ proposed the back-propagation (BP) algorithm based on the chain rule for the derivative, and the training of the multilayer perceptron (MLP) has since been possible and proven to have the power to solve nonlinear problems. The basic structure of the MLP is shown in Figure 1b, which has more than three layers, i.e., the input layer, output layer, and at least one hidden layer. Each node of the MLP receives the inputs from the previous layer and transfers its output to the nodes in the next layer. Instead of the step function, MLPs use a sigmoid as the activation function to map each node's output to the region of 0–1 nonlinearly. Today, these simple neural networks are still widely used and achieved considerable performance in many tasks such as spectra prediction.^{62,63} In 1989, LeCun et al.⁶⁴ proposed the CNN model and integrated it with the BP, “weight sharing” (1986) and max-pooling technique. As shown in Figure 1c, basic CNN for classification is stacked by several convolutional and pooling layers and then outputs by several fully connected layers. This is the first CNN model that can be directly fed with raw natural images instead of vectors, which have been successfully applied to recognize the handwritten digits and proven more efficient than the MLPs and other machine learning methods such as SVM.⁶⁵ Nonetheless, the neural networks fail to attract broad interests because of the notorious “gradient vanishing”⁶⁶ and “overfitting”⁶⁷ problems in training multilayer networks, which significantly hinders their performance and applications. In 2012, Krizhevsky et al.⁵¹ reported that using the rectified linear

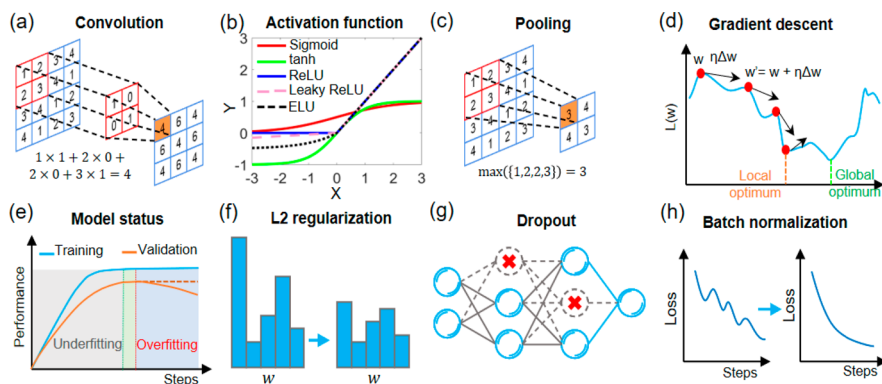


Figure 2. Basic concepts of deep learning: (a) convolution, (b) activation function, (c) pooling, (d) gradient descent, (e) model status, (f) L2 regularization, and (g) dropout. The dashed circles with a red cross indicate the turned-off neurons. (h) Batch normalization.

unit (ReLU) (Figure 2b, eq 3) as the activation function of CNNs could largely mitigate the gradient vanishing problem, which enables the training of deep models with a high learning efficiency. They also integrated the “dropout” and “data augmentation” to reduce the overfitting. Owing to the improvement in the two aspects, their 8-layers model AlexNet finally won the first place in the 2012 ILSVRC with a top-5 test error of 15.3%, which is much lower than the second place that with a top-5 test error of 26.2%. Since then, the deep CNNs have attracted huge attentions, and deep learning enters a new era. Unsurprisingly, artificial networks that are based on the CNN structure have swept all the ILSVRC awards in the next few years (2013–2017). In the 2014 ILSVRC, the very deep CNN model VggNet⁶⁸ (19 layers) and GoogLeNet⁶⁹ (22 layers) further decreased the classification error with a top-5 test error of 7.3% and 6.7%, respectively. The GoogLeNet improved the convolution layer with the “inception” module, which is a wide structure that can efficiently decrease the parameter number. In 2015, the residual learning⁷⁰ technique pushed the model to a much deeper level with a 152-layers ResNet and dramatically decreased the classification error down to 3.57%. It is widely accepted in the deep learning community that increasing the depth of the networks could endow it with more power in learning and predicting. However, as the model continues to deepen, its performance will saturate or even degrade. SENet⁷¹ (154 layers), which integrates a channel attention mechanism in each layer, shed a different light on improving the model capability, and surprisingly refreshed the record with a top-5 test error of 2.25% in the 2017 ILSVRC. Concurrent with the huge success in image classification, CNNs also achieved remarkable progress in other applications, such as the data generation, semantic segmentation, and image enhancement. U-Net,⁷² a pixel-to-pixel network, is proposed to the joint learning of localization and classification of biomedical images and has been the standard network architecture in many pixel-level image tasks. The generative adversarial network (GAN)⁷³ is an exciting breakthrough of deep learning in the data generation. Further modifications of GAN⁷⁴ make it a very versatile network architecture.

Basic Concepts of Deep Learning. Generally, there are four components in deep learning, i.e., deep learning model, loss function, optimization algorithm, and data set. The models have been intensively investigated in deep learning, and various architectures have been proposed. A deep learning model can be briefly treated as a “black box”, which receives an input and

then outputs an answer. There are three basic operations in a deep CNN model, the convolution (Figure 2a), activation (Figure 2b), and pooling (Figure 2c). Convolution extracts the feature maps from the inputs with a kernel matrix, of which the elements in the kernel are the trainable weights. The convolution can be 1-D, 2-D, or 3-D, with respect to different data types. 1-D convolution is applicable for the sequential data such as the spectra, whereas 2-D and 3-D convolution are applicable for the images or data cubes. Activation is first proposed to simulate the status (activated or nonactivated) of the neuron with a step function, then several activation functions are applied, such as the sigmoid (eq 1), tanh (eq 2), ReLU (eq 3), leaky ReLU (eq 4), and exponential linear unit (ELU) (eq 5).⁷⁵ The activation is to map its inputs into another space nonlinearly and is usually operated after the convolution. The responses of these activation functions are illustrated in Figure 2b. Pooling is a subsampling strategy, including max-pooling and average-pooling. Figure 2c illustrates the scheme of the max-pooling. Basically, a general CNN model, shown in Figure 1c, is mainly composed by several convolution, activation, and pooling layers and sometimes integrates several fully connected layers (i.e., the MLP).

$$f(x) = \frac{1}{1 + e^{-x}} \quad (1)$$

$$f(x) = \frac{e^x - e^{-x}}{e^x + e^{-x}} \quad (2)$$

$$f(x) = \max(0, x) \quad (3)$$

$$f(x) = \begin{cases} ax, & x < 0 \quad (a \geq 0) \\ x, & x \geq 0 \end{cases} \quad (4)$$

$$f(x) = \begin{cases} a(e^x - 1), & x < 0 \\ x, & x \geq 0 \end{cases} \quad (5)$$

The performance of the deep learning model can be evaluated by the loss function, $L(w)$, which can be viewed as an implicit function of the model weights. In short, the training of a neural network is to minimize the loss. During training, the prediction is compared with the true label to compute a loss. The loss is then backward propagated through the network to compute the gradients of the loss function and update the model weights. The loss function is typically optimized using a

Table 1. Loss Functions, Metrics, and Optimizers

tasks	loss functions	metrics	optimizers
classification	cross entropy weighted cross entropy	accuracy intersection over union (IOU)	
segmentation	focal loss; dice loss mean absolute error (MAE)	pixel accuracy signal-to-noise ratio (SNR)	stochastic gradient descent (SGD); RMSprop; Adam; Momentum
regression	mean square error (MSE)	peak signal-to-noise ratio (PSNR) structure similarity (SSIM)	

Table 2. Deep Learning Models in the Biospectroscopy and Biospectral Imaging Adopted in Literature

	general CNN (23)	ResNet (8)	U-Net (11)	GAN (12)	others (3)
preprocessing ^{77–94}	refs 77 and 78	refs 79–81	refs 82–86	refs 83, 84, 87–93	ref 94
feature detection ^{95–113}	refs 95–99	refs 100–103	refs 104–109	refs 110–112	ref 113
modeling ^{114–132}	refs 114–129	refs 130 and 131			ref 132

gradient-descent-based iterative optimization algorithm. As shown in Figure 2d, in each step, the current weight vector (red dot) is moved along the direction of steepest descent (direction arrow) and its amplitude is controlled by the learning rate (η). The loss function should be chosen appropriately in different tasks. Table 1 lists several common loss functions, metrics, and optimizers.

The model should be trained on an appropriate data set that is coupled with the training strategy, and the deep learning can be basically divided into three types according to different training strategies, i.e., the supervised learning, semisupervised learning, and unsupervised learning. In the supervised learning, the model is fed with annotated data. Whereas, if the model is trained by unlabeled data, the training is unsupervised. A compromise of these two strategies is the semisupervised learning, in which the model is trained by both annotated and unannotated data. Generally, for the same task, supervised learning shows the best performance, followed by semisupervised learning, and the unsupervised learning. In most cases of this Feature, we refer to the deep learning as supervised learning. Generally, the data set is split into three parts: training, validation, and testing data set. The training data set is used to tune the deep learning model, the validation data set is used to evaluate the model status (underfitting or overfitting) and tune the hyperparameters such as the learning rate and training epoch, and the test data set is used to evaluate the performance of the model in an unbiased manner. Unlike the cross validation, the validation in deep learning is usually external data set which will not been used to train the model.

During the training process of deep neural network, the “underfitting” and “overfitting” are the commonly encountered problems. The fitting status of the model can be indicated by the training and validation performance curves as shown in Figure 2e. The underfitting implies that the model could not converge to a global optimum on the validation data set that has not been used to train the model. Increasing the model parameter number is a common method to mitigate the underfitting. In contrast, the overfitting means that the model achieves good performance on the training data set but with poor generalization on the validation data set. The overfitting can be attributed to the high model complexity and the insufficient training data set. Accordingly, decreasing the parameter number and expanding the data set could be helpful to reduce the overfitting. Besides, several regularization tricks such as L2 regularization, dropout, and batch normalization can be used to reduce the overfitting. The L2 regularization

(Figure 2f, eq 6) adds a second order penalty terms ($\alpha \sum_W \omega^2$) to the loss function $J(W)$ that could help to flatten the weights (W) distribution during the training. The dropout (Figure 2g) randomly turns off some neurons in each training step, so that the model will not overly rely on any specific neuron to predict. The batch normalization⁷⁶ (Figure 2h, eq 7) shifts the “internal covariate” of each layer’s input into zero mean and standard variance, which can dramatically accelerate the convergence and regularize the model simultaneously. In eq 7, the u and σ^2 indicate the mean value and variance of the mini-batch input, respectively, γ and β are learning parameters.

$$\hat{J}(W) = J(W) + \alpha \sum_W \omega^2 \quad (6)$$

$$\text{BN}(x_i) = \gamma \frac{x_i - u}{\sqrt{\sigma^2 + \epsilon}} + \beta \quad (7)$$

Popular Deep Learning Models. In this section, we introduce the most widely used deep learning models in biospectroscopy and biospectral imaging. Table 2 illustrates an overview of recently published literature, and the number in the parentheses indicates the publication. It is clear that, so far, the general CNN, ResNet, U-Net, and GAN (including their variants) are the most widely adopted deep learning models.

General CNN models (Figure 1a), the simple variants of basic CNN, are versatile models in all the data processing phases because of the simple architecture and the ease of use. Particularly, they are the first choice in most of the modeling tasks (classification and regression). The only difference of the general CNN in different tasks is the final layer. For example, a fully connected layer is used in most cases of modeling tasks, whereas it will be replaced by a convolution layer in most data preprocessing and feature detection tasks to achieve the element-wise prediction.

ResNet for classification (Figure 3a) contains several residual units and outputs by the fully connected layer. Each residual unit contains several convolutional and activation layers. Most importantly, it has a short connection to directly pass the input information to the output of the unit. The short connection explicitly reformulate the layers as learning residual functions with reference to the input layers, instead of learning unreferenced functions. The residual unit fits $F(x_{l-1})$ to $x_l - x_{l-1}$, then the original mapping can be recast into $x_l = F(x_{l-1}) + x_{l-1}$. The explicit learning of the residual can significantly improve the performance and training efficiency for very deep CNNs. The residual learning strategy of ResNet has been

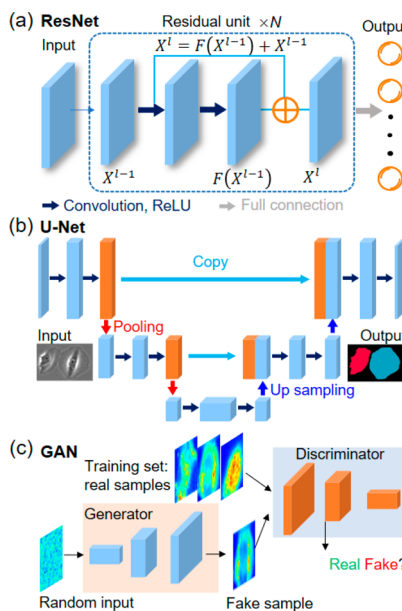


Figure 3. Popular deep CNN models. Each box corresponds to a multichannel feature map, and the arrows denote the operation. (a) ResNet for classification contains several “residual units” and output by a full connection layer. In each residual unit, the output x_i equals the input x_{i-1} plus the nonlinear mapping $F(x_{i-1})$ of the convolutional operation. (b) U-Net for segmentation is a pixel-wise model that receives an image as input and outputs a segmentation map, of which each pixel in the map corresponds to a subclass. (c) GAN contains two adversarial networks, i.e., the generator (G) and discriminator (D). Both of them can be an MLP or CNN structure.

extended to many other deep learning models, and various modified ResNet have been proposed.¹³³ The ResNets can be also applied to all the phases of the general data processing routine.

U-Net (Figure 3b) is an U-shaped pixel-wise CNN model. It has a similar symmetrical structure with the encoder-decoder networks, which gradually compresses the input into a latent space by pooling and then expands the features symmetrically by the up sampling. It mirrors the features from the shallow layers (left side) to the deep layers (right side) to provide better prediction ability for the border pixels of the input. It has excellent ability in pixel-wise tasks and has been widely used in the preprocessing and feature detection, such as image reconstruction and semantic segmentation. Taking segmentation as an example, the U-Net receives a cell image as the input and output of a segmentation map, of which each pixel indicates a subclass, say, background or cell.

GAN (Figure 3c) contains two adversarial networks, i.e., the generator (G) and discriminator (D). Both of them can be a MLP or CNN model. Taking sample generation as an example, G receives random inputs to produce fake samples that can fit the real sample distribution. D estimates the probability that a sample came from the real samples rather than G . The training procedure for G is to maximize the error of D for prediction. Given a distribution $Z \sim P_z$, G defines a probability distribution P_g as the distribution of the samples $G(Z)$. The objective of a GAN is to learn the generator’s distribution P_g that approximates the real data distribution P_r . Optimization of a GAN is performed with respect to a joint loss function for D and G as eq 8.

$$J(D, G) = E_{X \sim P_r} \log D(X) + E_{Z \sim P_z} [1 - \log G(Z)] \quad (8)$$

■ DEEP LEARNING APPLICATIONS

Here in this section, we briefly overview the applications of deep learning in the data preprocessing, feature detection, and modeling.

Deep Learning for Data Preprocessing. The data processing aims at improving the quality and reliability of the raw data by minimizing the insignificant variation or by

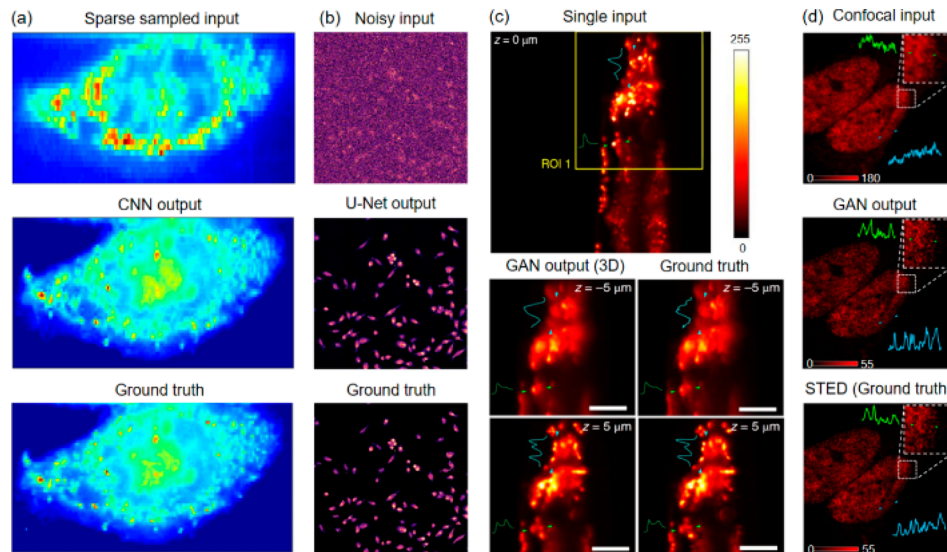


Figure 4. (a) CNN used for restoring the Raman image of a living CaSki cell in a line-scan Raman imaging system. Reproduced with permission from ref 134. Copyright 2019 American Chemical Society. (b) U-Net used for denoising the Raman image of MIA PaCa-2 cancer cells acquired with a stimulated Raman microscopy. Reproduced with permission from ref 86. Copyright 2019 Society of Photo-Optical Instrumentation Engineers. (c) GAN used for generating the 3D fluorescence image of *C. elegans* worm at different z -planes from a single wide-field fluorescent image. Reproduced with permission from ref 87. Copyright 2019 Springer Nature. (d) GAN used for generating STED image of Histone 3 distributions within HeLa cell nuclei based on the confocal image. Reproduced with permission from ref 91. Copyright 2019 Springer Nature.

enhancing the detailed information at the element-wise level. Conventionally, the data preprocessing of spectroscopic data includes background correction, noise reduction, and enhancement of spatial and spectral or temporal resolution. These tasks are usually difficult to obtain global optimal solution by the traditional computational methods because of their ill-posed nature. Basically, these methods are based on limited prior knowledge to constraint the potential solutions or blind regularization methods, which usually result in low fidelity. Deep learning, as an end-to-end, the data-driven method has shown its great power in solving these problems with the iterative learning strategy and its universal approximation ability. Compared with the traditional step-by-step data preprocessing procedure, deep learning directly learns the abundant implicit prior knowledge and hidden features from enormous data and thus can largely improve the data quality and meanwhile circumvent the user bias. In this section, we summarize the data preprocessing as two main subsets according to their targets, i.e., for improving the temporal resolution such as denoising, sparse sampling, and 3D reconstruction and for improving the lateral ($X-Y$) resolution.

Deep Learning for Improving Temporal Resolution. For any spectroscopic platform, a common dilemma in signal acquisition is the trade-off between speed and data quality (SNR, spectral, or spatial resolution, etc.). For instance, to obtain high SNR Raman images, long exposure time and high laser power are preferred. However, this strategy can only be applied to stable samples and for steady-state measurement. Similar challenge also lies in the 3D fluorescence imaging, which is usually realized by scanning an excitation source through the sample volume to obtain images at multiple planes. The multiple scan not only slows down the imaging speed but also brings problems from the mechanical scanning. Accordingly, a fast detection system is urgently required, especially for laser sensitive samples and dynamic tracking of bioevents to avoid phototoxicity, photobleaching, and imaging artifacts due to sample motion or drift. The computation-aided technique such as deep learning, has shown its great potential in speeding up the data acquisition of current microscopies in a cost-effective manner.

Among various methods, one elegant way is the sparse sampling, which speeds up the data acquisition by reducing the sampling rate and then retrieves the unsampled information through algorithms. Deep learning is also very helpful for this kind of tasks. For instance, we reported a sparse sampling strategy,¹³⁴ which used CNN to compensate the insufficient sampling to push the imaging speed limit of living cells on an already fast line-scan Raman imaging system. We used a wide slit and a large scan step to scan the sample in an overlapped manner to avoid the information loss and meanwhile reduce the imaging time. Furthermore, the wide slit allows more Raman signals to enter the spectrometer, which improves the sensitivity and reduce the exposure time for obtaining a high SNR spectra. As shown in Figure 4a, the degraded Raman images as a result of the sparse sampling are then input into a well-trained CNN model to retrieve corresponding high-resolution ones. Compared with the traditional line-scan Raman imaging, this method offers 5 times improvement in imaging speed and can be used to monitor the dynamic process of living cells which previously has been difficult.

Another popular method is to reduce the exposure time per scan to obtain relative low SNR data and then enhance them through denoising algorithms.^{82,86,135} For example, the Cheng

group⁸⁶ reported a 3D U-Net deep model which can leverage the spectral and spatial correlation contained in the stimulated Raman spectroscopy (SRS) image stacks and achieved an amazing denoising performance as shown in Figure 4b. They surprisingly found that the U-Net can differentiate the adjacent lipid droplets in the cell Raman image which is indiscernible in the state-of-the-art block-matching 4D filtering (BM4D) result. With this method, they achieved ultrafast data acquisition with a speed of $20\ \mu\text{s}$ per spectrum and 2 s per image stack. Bryce et al.⁸⁵ also used U-Net to denoise the SRS image of HeLa cell. U-Net shows superior fidelity with 2.89 times higher PSNR than the state-of-the-art conventional variance stabilization transform (VST) method.

The 3D reconstruction provides an alternative choice for speeding up the 3D imaging, especially in fluorescence microscopies. For example, Wu et al.⁸⁷ proposed a deep-learning-based approach, Deep-Z (conditional GAN model), to achieve 3D fluorescence imaging through a single wide-field image, without the need of mechanical scanning and additional hardware. The Deep-Z was trained with various matched pairs of fluorescence images axially focused at different depths and ground truth images acquired at different focus planes. As shown in Figure 4c, they demonstrated the 3D imaging of *Caenorhabditis elegans* neurons through the Deep-Z, which accurately output high fidelity fluorescence images at different focus planes of $Z = -5\ \mu\text{m}$ and $Z = +5\ \mu\text{m}$ from a single image acquired at $Z = 0\ \mu\text{m}$. This method is capable of increasing the depth of field (DOF) of a standard wide-field fluorescence microscope by \sim 20-fold with only a single shot imaging.

Deep Learning for Improving Lateral Resolution. Obtaining detailed spatial information on the sample is of great importance for a wide range of research such as understanding the subcellular structure and regulation mechanism of biomolecules. However, for the conventional microscopies, the spatial resolution is confined by the optical diffraction limit, corresponding to about half the wavelength. Fortunately, the super-resolution microscopies, such as stimulated emission depletion (STED), structured illumination microscopy (SIM), photoactivated localization microscopy (PALM), and stochastic optical reconstruction microscopy (STORM), provide alternative choices to easily achieve a spatial resolution well below the diffraction limit (down to tens of nanometers).⁹⁴ Thanks to these well-developed techniques, the inner structure of cells and various biological processes can be recorded. However, these methods highly rely on sophisticated optical setups and are too expensive to broad applications. Deep-learning-based super-resolution microscopy, provides a cost-effective way to obtain super-resolved images from the diffraction-limited ones. For example, Wang et al.⁹¹ reported a GAN model to reconstruct super-resolution fluorescence images from diffraction-limited confocal microscopy image (Figure 4d). With this method, the lateral resolution of the confocal fluorescence microscope with an emission wavelength of 645 nm can be significantly improved from \sim 290 nm to \sim 110–120 nm, comparable to that of a STED microscope. The GAN also could map the wide-field images acquired with low-numerical-aperture ($10\times/0.4\text{-NA}$) into high-numerical-aperture ($20\times/0.75\text{-NA}$) ones without the need of numerical modeling. This enables the acquisition of high-resolution images with the large field of view (FOV) of the low NA objectives. Zhang et al.⁸⁹ generated high-resolution ($\sim 1.7\ \mu\text{m}^2$) images with large FOV ($95\ \text{mm}^2$) from low-resolution ones without the need to change the setup of the microscope.

With this technique, the sophisticated multiple scans, aligning and stitching of multiple high-resolution tiles can be circumvented. These examples indicate that the deep learning can greatly improve the current spectroscopic platforms in a parameter-free way and can serve to democratize the super-resolution imaging.

Deep Learning for Feature Detection. Feature detection is the successive step after the data preprocessing, which aims at extracting the most interested information on the data. Conventional manual feature selection requires for domain expertise and sample-dependent tuning which is usually time-consuming and cost-demanding. Deep-learning-based methods could largely mitigate these limitations and have achieved tremendous success especially in feature detection. Here in this section, we briefly review the applications of deep learning in semantic segmentation and digital staining.

Semantic Segmentation. The precise localization and segmentation of bioimages are crucial to understand the physiology at the tissue or cellular level to provide decision-making evidence for preoperative or intraoperative tumor identification.^{100,108} A vast amount of methods have been proposed to automate image segmentation. The majority of them are based on handcrafted features,¹¹³ such as the intensity thresholding, morphological filtering, region accumulation, deformable model fitting, and marker controlled watershed.^{136,137} However, many of them require human interference,⁵⁰ leading to poor general applicability due to the substantial variance of different biosamples and instrumental platforms. As an alternative, the deep learning can automatically extract optimal features to circumvent the manual selection of features and meanwhile achieve state-of-the-art accuracy. For example, Trajanovski et al.¹³⁸ combined U-Net and visual (VIS) and near-infrared (NIR) to perform tongue tumor semantic segmentation. The VIS and NIR images are synthesized as a hypercube of the U-Net input. Then the model outputs the segmented map to clearly delineate the cancer and normal tissue interface (Figure 5a). They surprisingly found that the segmentation based on the hyperspectral imaging (HSI) data shows significantly better performance than that of the RGB based one. Their fine-tuned U-Net model finally achieved an average accuracy of 0.958 on the clinical data set (14 patient, 7-fold cross validation) with tongue squamous cell carcinoma. This spectroscopic and deep learning assisted semantic segmentation technique shows a huge potential to be a promising alternate to digital pathology or a doctor's supportive tool in real-time surgeries. Hollon et al.¹⁰⁰ combined stimulated Raman histology (SRH) and CNN to perform near real-time intraoperative brain tumor diagnosis. They demonstrated that the well-trained CNN (based on ResNet) directly output a tumor probability heatmap from the SRH image (synthesized with the Raman images acquired at 2845 cm^{-1} and 2930 cm^{-1}) of a grade I meningioma tissue. The brain–tumor interface can be well delineated using CNN semantic segmentation and shows high consistency with the ground truth. The method enables accurate tumor segmentation and can be used to intraoperatively identify diagnostic regions, residual tumor burden, and tumor margins. Todorov et al.⁹⁶ developed a deep-learning-based framework named Vessel Segmentation & Analysis Pipeline (VesSAP) to quantify and analyze the mouse brain vasculature with a 3D light sheet fluorescence microscopy. Their 3D CNN model achieved human level accuracy despite the variations in signal intensities

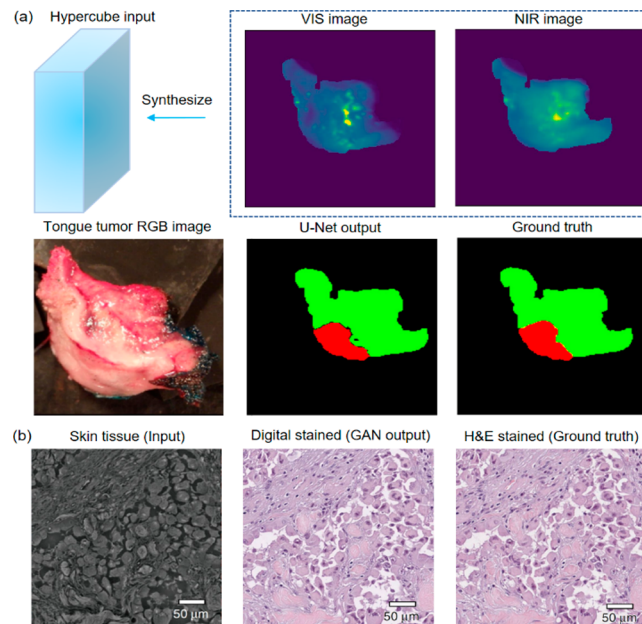


Figure 5. (a) Semantic segmentation of tongue tumor by U-Net. Top row: the synthesized hypercube by the VIS and NIR hyperspectral images. Second row, from left to right: the RGB image of tongue tissue, the segmented map output by U-Net, the ground truth (the green color indicates normal tissue; red indicates cancer). Reproduced with permission from ref 138. Copyright 2019 IEEE. (b) Digital staining of a salivary gland tissue by GAN. From left to right: QPI image, the virtual hematoxylin and eosin (H&E) stained image output by the GAN, the H&E histologically stained image. Reproduced with permission from ref 112. Copyright 2019 Springer Nature.

and structures and can be used for the entire mouse brain vasculature segmentation and automatic localization. The VesSAP achieved an overall accuracy of 0.94 on a test data set containing 75 volumes of $100 \times 100 \times 50$ pixels, which outperformed the state-of-the-art classical methods far better (0.84–0.86).

Digital Staining. Histological stains, such as hematoxylin and eosin (H&E), Jones stain, and Masson's trichrome, are the routinely used gold standards in clinical diagnosis and research.¹¹¹ However, these histological stain methods usually involve lengthy and laborious tissue preparation. Furthermore, as a result of the chemical stains, the downstream analysis of the sample is usually impossible since the dyes will permanently alter the tissue.⁹⁹ The recently developed deep-learning-based digital staining provides a superior alternative for the fast and label-free tissue histological staining, which leverages the machine learning to transform the microscopy images to chemically stained ones. Rivenson et al.^{111,112,139} pioneered the digital staining with deep learning. They demonstrated that a well-trained GAN can transform both quantitative phase images¹¹² (QPI) (Figure 5b) and wide-field autofluorescence images¹¹¹ of unlabeled tissue sections into images that are equivalent to the bright-field images of histologically stained ones. They further sent both the digital stained and histologically stained images of 15 tissue sections to four broad-certified pathologists who were unaware of the digital staining. No significant difference in diagnosis has been identified by those professional pathologists. With this technique, the step-by-step procedure and human-to-human variation at different stages of the sample preparation can be circumvented. Once the deep learning model is well-trained, it

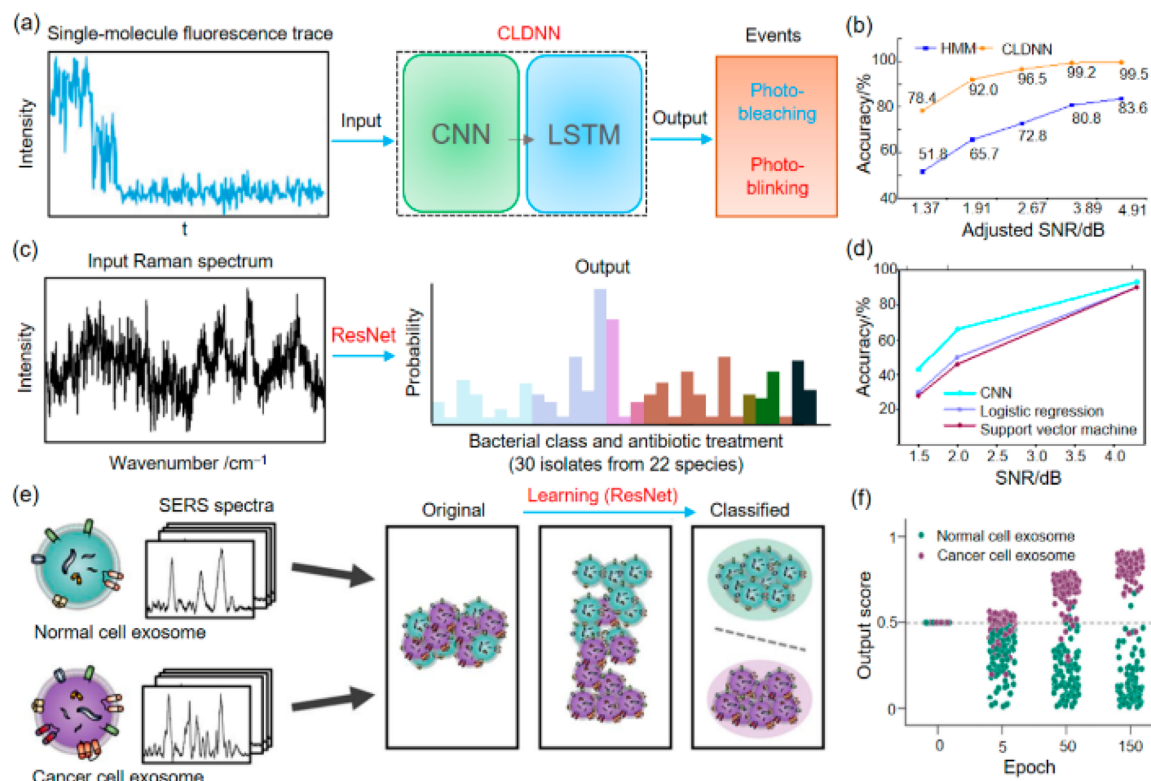


Figure 6. (a) Scheme for differentiating the photobleaching and photoblinking of single molecule via fluorescence traces and CLDNN. (b) Dependence of identification accuracy on the adjusted-SNR obtained by the CLDNN and HMM methods. Reproduced with permission from ref 141. Copyright 2019 American Chemical Society. (c) Scheme of bacterial identification via Raman spectroscopy and deep learning. (d) Dependence of identification accuracy on the SNR of bacteria Raman spectra obtained by CNN, LR, and SVM. Reproduced with permission from ref 130. Copyright 2019 Springer Nature. (e) Scheme for cancer cell exosome identification via SERS and deep learning. (f) Final output score of 200 representative SERS spectra by training iterations. Reproduced with permission from ref 142. Copyright 2020 American Chemical Society.

can rapidly output the digital stained images, for example, 1.9 s mm^{-2} using a dual-GPU desktop computer for unstained tissue slides using a $20\times$ objective. In contrast, it takes on average from 45 min to 3 h with an estimated cost of US \$2–35 for each conventional histological staining procedure for a tissue section. Lotfollahi et al.⁹⁸ also reported deep-learning-based digital staining that accurately produces virtual stained H&E slides from the Fourier transform IR microscopy images. With this method, the high-definition digital staining of the tissue section at the cellular level can be achieved.

Deep Learning for Modeling. Modeling is the final stage of the general data processing routine in spectral analysis, including regression (quantitative analysis) and classification (qualitative analysis). Among them, classification has been intensively researched. In this section, we briefly review the recent works of deep learning in the classification of spectral data in biological systems.

Spectroscopic-based classification has been the most widely used qualitative analysis tool. So far, low SNR and high complexity of the biospectral data are the two commonly encountered problems in qualitative analysis, which have caused a great obstacle for classification. Deep learning offers superior performance and robustness over the traditional algorithms and enables it to mitigate the above limitations and to be applicable in various biomedical applications ranging from the single molecular^{117,140,141} to the cellular^{121,129} and tissue levels.^{101,119,131}

For example, the Fang group¹⁴¹ reported a convolutional and long-short-term memory (LSTM) deep learning neural

network (CLDNN) to classify the photobleaching and photoblinking of a single-molecule in a living HeLa cell (Figure 6a). The time-dependent fluorescence intensity traces of interested molecules were acquired by a total internal reflection fluorescence microscope (TIRFM), which were input to the CLDNN model to detect the photobleaching for the downstream analysis of protein stoichiometry. As indicated in the adjusted-SNR-dependent accuracy curves in Figure 6b, the CLDNN shows much higher noise resistance ability over the traditional hidden Markov model (HMM). This method offers an advantageous alternate for detecting photobleaching at the single molecular level, which has been difficult previously due to the extremely low SNR and interference coming from the photoblinking.

Dionne et al.¹³⁰ used ResNet and Raman spectroscopy for fast identification of 30 pathogenic bacteria isolates from 22 species (Figure 6c). ResNet is capable of accurately identifying low SNR spectra and outperforms the traditional LR and SVM method, which can be observed from the SNR-dependent accuracy curves in Figure 6d. The Raman spectra for testing were acquired at a short integration time of 1 s, corresponding to a low SNR of 4.1 dB, which is roughly an order of magnitude lower than the typical reported bacterial spectra. Even on the basis of such a low SNR data set (100 spectra each isolate), the model achieved an average accuracy of exceeding 82% on the identification task of 30-class isolates. Moreover, they validated the fine-tuned model on the clinical isolates from 50 patients and surprisingly achieved a treatment identification accuracy of 99.7%, using only 10 bacterial

spectra from each patient isolate. This deep learning assisted approach shows the potential of culture-free pathogen identification and can be applicable in practical diagnosis.

Shin et al.¹⁴² also used ResNet-based method to detect the early stage lung cancer through the identification of surface enhanced Raman scattering (SERS) spectra of cell exosomes (Figure 6e). Exosomes are nanosized (30–200 nm) extracellular vesicles derived from the blood, which are considered to be the most important biomarkers of lung cancer. They first trained the network with an annotated SERS data set (1125 cancer spectra, 1025 normal spectra) acquired from the cell line-derived exosomes. As indicated in Figure 6f, the spectra can be well separated into two groups after 150 training epochs. Their model achieved an accuracy of 95% on the test set (430 spectra) and finally an area of curve (AUC) of 0.912 on the real data set acquired from much more complex and heterogeneous human plasma derived exosomes (43 patients). In contrast, the AUCs of the traditional PCA-DA, PLS-DA, and SVM models on the real human derived exosomes data set are less than 0.8. This fact indicates the high accuracy and robustness of the ResNet model in handling complex spectral data. This deep learning-assisted SERS classification technique shows promising potential for the detection of early stage lung cancer.

Recently, there are increasing reports of using deep learning and spectroscopic techniques to identify the human derived samples at the single cellular level^{114,121,128,129,143} and tissue level.^{99,115,131} This trend indicates the great potential of deep-learning-assisted spectroscopic qualitative analysis in various biomedical research studies.

CHALLENGES AND OUTLOOK

Deep learning has revolutionized the data processing and been proven to be a very powerful tool for biospectroscopy and biospectral imaging. Deep models based on the CNN architecture have been found particularly effective due to their capacity to extract highly abstract features and effectively leverage the morphological and spectral information within the hyperspectral data. Concurrent with these benefits, several challenges should be overcome to further exert the potential of deep learning. Here in this section, we briefly discuss the challenges in aspects of the data set and interpretability of deep learning and the outlook of the future of deep learning for spectroscopic application.

Challenges Related to the Data Set. There is an increasing need of deep learning in various spectroscopic-based biomedical applications. However, further development has been hindered by the data shortage.¹⁴⁴ Two main reasons have led to this problem. First, obtaining the spectroscopic data of the biosamples requires complicated sample preparations and instrumental operations, which is time-consuming and cost-demanding. Second, the massive labeling of the spectroscopic data is difficult especially for the living samples. Particularly, some dynamic systems require the training data pairs acquired by two or more successive experiments. At present, data augmentation is a widely adopted method to compensate the problem when large data sets are unavailable.⁵⁶ Although, this method could slightly improve the model performance, it cannot ultimately solve the problem of data shortage. Therefore, it is important to develop deep models that can be trained on small data sets. In this regard, “few-shot learning”^{145,146} could be a promising direction. The term “few-shot learning” is borrowed from the human learning which

allows one to learn new concepts from just a few examples.¹⁴⁷ Similarly, in few-shot learning, the model is first trained on the annotated classes and then learns to recognize new classes with only a few examples per class. It aims at endowing artificial intelligent systems with a similar ability. Yet, it is still too preliminary to be applicable. Another alternative solution is the transfer learning which has been intensively adopted especially in the computer vision. However, transfer learning relies on an appropriate large data set such as ImageNet to offer pretrained knowledge that can be transferred to similar tasks. Such a spectroscopic data set is still unavailable due to the complexity of biosamples and variation of instruments. Therefore, it requires a concerted effort to produce large curated data sets that can meet the various needs of spectral analysis. The open-access data sets not only provide an alternative way to some typical circumstances where large data sets are unavailable but also serve as the standards to help the evaluation of various models.

Interpretability of the Black Box. In traditional science, a decision-making system should offer apparent evidence to interpret the results. However, the black box nature of the deep learning makes the interpretability impossible, which has been the most controversial issue.¹⁴⁸ It has been with common sense that we must build transparent models which can explain why they predict and what they predict. Particularly, the trust in the deep models must be established before they can be deployed in the healthcare systems. Zhang et al. managed to decipher the black box by the gradient backprop-based methods, such as gradient weighted class activation mapping,¹⁴⁹ excitation backprop.¹⁵⁰ The main idea of these methods is to produce a coarse localization map highlighting the important regions in the input image, which can provide visual explanation in the image classification tasks. Still, the attempt to improve the interpretability of the deep learning model is in its infant stage and more attention should be paid to this issue.

Unsupervised Learning. Unsupervised learning is a promising future direction for deep learning. The unsupervised nature enables it to circumvent the massive annotation of supervised learning, endowing it with broad potential applications in various fields. It had played a significant role in the reviving of deep learning before 2012.¹⁵¹ Thereafter, it has been shadowed by the tremendous success of supervised learning.⁵² So far, the main application of unsupervised learning is limited to the pretraining (denoising or dimension reduction),¹⁵² which serves the downstream tasks for further fine-tuning. Nevertheless, the efforts in unsupervised learning have never been given up. For example, the recently developed momentum contrast (MoCo)¹⁵³ method for unsupervised learning outperformed the counterpart supervised model in several visual tasks such as object detection and segmentation. This result indicates that the performance of unsupervised learning can be comparable to supervised learning through a well-designed learning strategy. We expect the unsupervised learning to become far more powerful and versatile in handling the spectroscopic data in the near future.

AUTHOR INFORMATION

Corresponding Authors

Lei Wang – School of Aerospace Engineering, Xiamen University, Xiamen 361000, China;  orcid.org/0000-0001-7276-0832; Email: wanglei33@xmu.edu.cn

Bin Ren – State Key Laboratory of Physical Chemistry of Solid Surfaces, Collaborative Innovation Center of Chemistry for

Energy Materials (iChEM), College of Chemistry and Chemical Engineering, Xiamen University, Xiamen 361005, China;  orcid.org/0000-0002-9821-5864; Email: bren@xmu.edu.cn

Authors

Hao He – School of Aerospace Engineering, Xiamen University, Xiamen 361000, China

Sen Yan – State Key Laboratory of Physical Chemistry of Solid Surfaces, Collaborative Innovation Center of Chemistry for Energy Materials (iChEM), College of Chemistry and Chemical Engineering, Xiamen University, Xiamen 361005, China

Danya Lyu – State Key Laboratory of Physical Chemistry of Solid Surfaces, Collaborative Innovation Center of Chemistry for Energy Materials (iChEM), College of Chemistry and Chemical Engineering, Xiamen University, Xiamen 361005, China

Mengxi Xu – State Key Laboratory of Physical Chemistry of Solid Surfaces, Collaborative Innovation Center of Chemistry for Energy Materials (iChEM), College of Chemistry and Chemical Engineering, Xiamen University, Xiamen 361005, China

Ruiqian Ye – School of Aerospace Engineering, Xiamen University, Xiamen 361000, China

Peng Zheng – School of Aerospace Engineering, Xiamen University, Xiamen 361000, China

Xinyu Lu – State Key Laboratory of Physical Chemistry of Solid Surfaces, Collaborative Innovation Center of Chemistry for Energy Materials (iChEM), College of Chemistry and Chemical Engineering, Xiamen University, Xiamen 361005, China

Complete contact information is available at:

<https://pubs.acs.org/10.1021/acs.analchem.0c04671>

Notes

The authors declare no competing financial interest.

Biographies

Hao He is pursuing his Ph.D. degree in School of Aerospace Engineering at Xiamen University with Professor Lei Wang. His research topics are focused on deep learning and hyperspectral imaging.

Sen Yan is pursuing his Ph.D. degree in the College of Chemistry and Chemical Engineering at Xiamen University with Professor Bin Ren. His research interests are focused on surface-enhanced Raman spectroscopy and single molecule detection.

Danya Lyu is a postdoctoral fellow working with Professor Bin Ren in Department of Chemistry at Xiamen University. She received her Ph.D. degree in Analytical Chemistry at Nankai University in 2018. Her research interests are focused on electroanalysis and SERS-based protein analysis.

Mengxi Xu is pursuing his Ph.D. degree in the College of Chemistry and Chemical Engineering at Xiamen University with Professor Bin Ren. His research interests are focused on *in situ* investigation and data analysis of live-cell processes by spontaneous and surface-enhanced Raman spectroscopy.

Ruiqian Ye is pursuing his Master's degree in the School of Aerospace Engineering at Xiamen University with Professor Lei Wang. His research is focused on signal analysis and image processing.

Peng Zheng is pursuing his Ph.D. studies in the School of Aerospace Engineering at Xiamen University with Professor Lei Wang. His

research topic is focused on deep learning and super-resolution imaging.

Xinyu Lu is pursuing his Master studies in the College of Chemistry at Xiamen University with Professor Bin Ren. His research topic is focused on spectral classification.

Lei Wang is an Associate Professor in School of Aerospace Engineering at Xiamen University. He obtained his B.S. (1997) and Master's (2002) in the Department of Instruments at Xiamen University and a Ph.D. (2007) degree in the Department of Computer Science at Hefei University of Technology. His research focuses on the application of artificial intelligence in image processing, chemometrics, bioimaging, and Raman imaging.

Bin Ren received his B.S. (1992) and Ph.D. (1998) degrees in the Department of Chemistry at Xiamen University in 1998. He then became an Assistant Professor (1998), Associate Professor (2000), and Full Professor (2004) in the same department. He has been a Changjiang Scholar Professor of Xiamen University from 2016. He spent a sabbatical year as an Alexander von Humboldt fellow in the Fritz-Haber Institute MPG on TERS during 2002–2003. He is now a Vice Director of the State Key Laboratory of Physical Chemistry of Solid Surfaces, a Vice Dean of the College of Chemistry and Chemical Engineering, and an Associate Editor of *Analytical Chemistry*. His current interests are focused on nanoplasmatics, surface-enhanced Raman spectroscopy, tip-enhanced Raman spectroscopy, and their application in surfaces and interfaces of electrochemical and biological systems with emphasis on developing methodologies and instruments.

ACKNOWLEDGMENTS

The authors acknowledge the financial supports from NSFC (Grants 22021001, 21790354, and 21633005), MOST of China (Grant 2016YFA0200601), “111” Project (Grant B08027), and the China Postdoctoral Science Foundation (Grant 2019M662230).

REFERENCES

- (1) Cheng, J. X.; Xie, X. S. *Science* **2015**, *350*, No. aaa8870.
- (2) Krafft, C.; Popp, J. *Anal. Bioanal. Chem.* **2015**, *407*, 699–717.
- (3) Chen, H.; Lin, Z.; Tan, C. *Microchem. J.* **2019**, *144*, 489–494.
- (4) Eberhardt, K.; Beleites, C.; Marthandan, S.; Matthaus, C.; Diekmann, S.; Popp, J. *Anal. Chem.* **2017**, *89*, 2937–2947.
- (5) Horton, N. G.; Wang, K.; Kobat, D.; Clark, C. G.; Wise, F. W.; Schaffer, C. B.; Xu, C. *Nat. Photonics* **2013**, *7*, 205–209.
- (6) Stelzer, E. H. K. *Nat. Methods* **2015**, *12*, 23–26.
- (7) Singh, G. A. P.; Gupta, P. K. *Neural Comput. Appl.* **2019**, *31*, 6863–6877.
- (8) Wang, W.; Zhao, J.; Short, M.; Zeng, H. *J. Biophotonics* **2015**, *8*, 527–45.
- (9) Yi, L.; Dong, N.; Yun, Y.; Deng, B.; Ren, D.; Liu, S.; Liang, Y. *Anal. Chim. Acta* **2016**, *914*, 17–34.
- (10) Angermueller, C.; Parnamaa, T.; Parts, L.; Stegle, O. *Mol. Syst. Biol.* **2016**, *12*, 878.
- (11) Pavillon, N.; Hobro, A. J.; Akira, S.; Smith, N. I. *Proc. Natl. Acad. Sci. U. S. A.* **2018**, *115*, E2676–E2685.
- (12) Esteki, M.; Shahsavari, Z.; Simal-Gandara, J. *Food Control* **2018**, *91*, 100–112.
- (13) Díez-Pastor, J. F.; Jorge-Villar, S. E.; Arnaiz-González, Á.; García-Osorio, C. I.; Díaz-Acha, Y.; Campeny, M.; Bosch, J.; Melgarejo, J. C. *J. Raman Spectrosc.* **2020**, *51*, 1563–1574.
- (14) Beier, B. D.; Quivey, R. G.; Berger, A. J. *J. Biomed. Opt.* **2010**, *15*, 066001.
- (15) Szymańska, E.; Gerretzen, J.; Engel, J.; Geurts, B.; Blanchet, L.; Buydens, L. M. C. *TrAC, Trends Anal. Chem.* **2015**, *69*, 34–51.
- (16) Carey, C.; Boucher, T.; Mahadevan, S.; Bartholomew, P.; Dyar, M. D. *J. Raman Spectrosc.* **2015**, *46*, 894–903.

- (17) Brownfield, B.; Lemos, T.; Kalivas, J. H. *Anal. Chem.* **2018**, *90*, 4429–4437.
- (18) Gonzalez-Durruthy, M.; Monserrat, J. M.; Rasulev, B.; Casanola-Martin, G. M.; Barreiro Sorrius, J. M.; Paraiso-Medina, S.; Maojo, V.; Gonzalez-Diaz, H.; Pazos, A.; Munteanu, C. R. *Nanomaterials* **2017**, *7*, 386.
- (19) Sevetlidis, V.; Pavlidis, G. *J. Cult Herit* **2019**, *37*, 121–128.
- (20) Held, M.; Schmitz, M. H.; Fischer, B.; Walter, T.; Neumann, B.; Olma, M. H.; Peter, M.; Ellenberg, J.; Gerlich, D. W. *Nat. Methods* **2010**, *7*, 747–54.
- (21) Ryabchikov, O.; Bräutigam, K.; Galler, K.; Neugebauer, U.; Mosig, A.; Bocklitz, T.; Popp, J. *J. Raman Spectrosc.* **2018**, *49*, 935–942.
- (22) Isozaki, A.; Mikami, H.; Hiramatsu, K.; Sakuma, S.; Kasai, Y.; Iino, T.; Yamano, T.; Yasumoto, A.; Oguchi, Y.; Suzuki, N.; Shirasaki, Y.; Endo, T.; Ito, T.; Hiraki, K.; Yamada, M.; Matsusaka, S.; Hayakawa, T.; Fukuzawa, H.; Yatomi, Y.; Arai, F.; Di Carlo, D.; Nakagawa, A.; Hoshino, Y.; Hosokawa, Y.; Uemura, S.; Sugimura, T.; Ozeki, Y.; Nitta, N.; Goda, K. *Nat. Protoc.* **2019**, *14*, 2370–2415.
- (23) Ogi, H.; Moriwaki, S.; Kokubo, M.; Hikida, Y.; Itoh, K. *Sci. Rep.* **2019**, *9*, 633.
- (24) Neugebauer, U.; Clement, J. H.; Bocklitz, T.; Krafft, C.; Popp, J. *J. Biophotonics* **2010**, *3*, 579–87.
- (25) Neugebauer, U.; Bocklitz, T.; Clement, J. H.; Krafft, C.; Popp, J. *Analyst* **2010**, *135*, 3178–82.
- (26) Li, X.; Yang, T.; Li, S.; Wang, D.; Song, Y.; Zhang, S. *Laser Phys.* **2016**, *26*, 035702.
- (27) Moawad, A. A.; Silge, A.; Bocklitz, T.; Fischer, K.; Rosch, P.; Roesler, U.; Elschner, M. C.; Popp, J.; Neubauer, H. *Molecules* **2019**, *24*, 4516.
- (28) Brauchle, E.; Thude, S.; Brucker, S. Y.; Schenke-Layland, K. *Sci. Rep.* **2015**, *4*, 4698.
- (29) Haka, A. S.; Shafer-Peltier, K. E.; Fitzmaurice, M.; Crowe, J.; Dasari, R. R.; Feld, M. S. *Proc. Natl. Acad. Sci. U. S. A.* **2005**, *102*, 12371–12376.
- (30) Fang, T.; Li, Y.; Li, F.; Huang, F. *Anal. Lett.* **2018**, *51*, 1400–1416.
- (31) Rau, J. V.; Marini, F.; Fosca, M.; Cippitelli, C.; Rocchia, M.; Di Napoli, A. *Talanta* **2019**, *194*, 763–770.
- (32) Lasch, P.; Stammler, M.; Zhang, M.; Baranska, M.; Bosch, A.; Majzner, K. *Anal. Chem.* **2018**, *90*, 8896–8904.
- (33) Chen, H.; Li, X.; Broderick, N.; Liu, Y.; Zhou, Y.; Han, J.; Xu, W. *J. Biophotonics* **2018**, *11*, No. e201800016.
- (34) Kong, K.; Rowlands, C. J.; Varma, S.; Perkins, W.; Leach, I. H.; Kolodydenko, A. A.; Williams, H. C.; Notingher, I. *Proc. Natl. Acad. Sci. U. S. A.* **2013**, *110*, 15189–94.
- (35) Kong, K.; Kendall, C.; Stone, N.; Notingher, I. *Adv. Drug Delivery Rev.* **2015**, *89*, 121–34.
- (36) Muro, C. K.; de Souza Fernandes, L.; Lednev, I. K. *Anal. Chem.* **2016**, *88*, 12489–12493.
- (37) Ksiazek, K.; Romaszewski, M.; Glomb, P.; Grabowski, B.; Cholewa, M. *Sensors* **2020**, *20*, 6666.
- (38) Doty, K. C.; Lednev, I. K. *TrAC, Trends Anal. Chem.* **2018**, *103*, 215–222.
- (39) Casey, T.; Mistek, E.; Halámková, L.; Lednev, I. K. *Vib. Spectrosc.* **2020**, *109*, 103065.
- (40) Byrne, H. J.; Knief, P.; Keating, M. E.; Bonnier, F. *Chem. Soc. Rev.* **2016**, *45*, 1865–78.
- (41) Tauler, R.; Parastar, H. *Angew. Chem., Int. Ed.* **2018**, DOI: 10.1002/anie.201801134.
- (42) Krauß, S. D.; Yosef, H. K.; Lechtenon, T.; Jütte, H.; Tannapfel, A.; Käfferlein, H. U.; Brüning, T.; Roghmann, F.; Noldus, J.; El-Mashtoly, S. F.; Gerwert, K.; Mosig, A. *J. Chemom.* **2018**, *32*, e2973.
- (43) Carrasquilla, J.; Melko, R. G. *Nat. Phys.* **2017**, *13*, 431–434.
- (44) Castelvecchi, D. *Nature* **2015**, *528*, 18–19.
- (45) Mater, A. C.; Coote, M. L. *J. Chem. Inf. Model.* **2019**, *59*, 2545–2559.
- (46) Schutt, K. T.; Gastegger, M.; Tkatchenko, A.; Muller, K. R.; Maurer, R. *J. Nat. Commun.* **2019**, *10*, 5024.
- (47) Zhang, Z. H.; Schott, J. A.; Liu, M. M.; Chen, H.; Lu, X. Y.; Sumpter, B. G.; Fu, J.; Dai, S. *Angew. Chem., Int. Ed.* **2019**, *58*, 259–263.
- (48) Mandal, S.; Greenblatt, A. B.; An, J. *IEEE Pulse* **2018**, *9*, 16–24.
- (49) Esteva, A.; Kuprel, B.; Novoa, R. A.; Ko, J.; Swetter, S. M.; Blau, H. M.; Thrun, S. *Nature* **2017**, *542*, 115.
- (50) Åkerberg, A. A.; Burns, C. E.; Burns, C. G.; Nguyen, C. *Dis. Models Mech.* **2019**, *12*, dmm040188.
- (51) Krizhevsky, A.; Sutskever, I.; Hinton, G. E. *Commun. ACM* **2017**, *60*, 84–90.
- (52) LeCun, Y.; Bengio, Y.; Hinton, G. *Nature* **2015**, *521*, 436–44.
- (53) Paoletti, M. E.; Haut, J. M.; Plaza, J.; Plaza, A. *Isprs J. Photogramm.* **2019**, *158*, 279–317.
- (54) Ralbovsky, N. M.; Lednev, I. K. *Chem. Soc. Rev.* **2020**, *49*, 7428.
- (55) Ralbovsky, N. M.; Lednev, I. K. *Spectrochim. Acta, Part A* **2019**, *219*, 463–487.
- (56) Pradhan, P.; Guo, S.; Ryabchikov, O.; Popp, J.; Bocklitz, T. W. *J. Biophotonics* **2020**, *13*, No. e201960186.
- (57) Hassan, J.; Shoaib, U. *Neural Process Lett.* **2020**, *51*, 1031–1048.
- (58) Sarikaya, R.; Hinton, G. E.; Deoras, A. *IEEE-ACM T Audio, Spe* **2014**, *22*, 778–784.
- (59) Rosenblatt, F. *Psychol Rev.* **1958**, *65*, 386–408.
- (60) Shrestha, A.; Mahmood, A. *IEEE Access* **2019**, *7*, 53040–53065.
- (61) Rumelhart, D. E.; Hinton, G. E.; Williams, R. J. *Nature* **1986**, *323*, 533–536.
- (62) Ye, S.; Hu, W.; Li, X.; Zhang, J.; Zhong, K.; Zhang, G.; Luo, Y.; Mukamel, S.; Jiang, J. *Proc. Natl. Acad. Sci. U. S. A.* **2019**, *116*, 11612–11617.
- (63) Ye, S.; Zhong, K.; Zhang, J.; Hu, W.; Hirst, J. D.; Zhang, G.; Mukamel, S.; Jiang, J. *J. Am. Chem. Soc.* **2020**, *142*, 19071–19077.
- (64) LeCun, Y.; Boser, B.; Denker, J. S.; Henderson, D.; Howard, R. E.; Hubbard, W.; Jackel, L. D. *Neural Comput* **1989**, *1*, 541–551.
- (65) Lecun, Y.; Bottou, L.; Bengio, Y.; Haffner, P. *Proc. IEEE* **1998**, *86*, 2278–2324.
- (66) Bengio, Y.; Simard, P.; Frasconi, P. *IEEE T Neur Net Lear* **1994**, *5*, 157–166.
- (67) Dietterich, T. *AcM Comput. Surv* **1995**, *27*, 326–327.
- (68) Simonyan, K.; Zisserman, A. *arXiv* **2014**, 1409.1556.
- (69) Szegedy, C.; Liu, W.; Jia, Y.; Sermanet, P.; Reed, S.; Anguelov, D.; Erhan, D.; Vanhoucke, V.; Rabinovich, A. *arXiv* **2014**, 1409.4842.
- (70) He, K. M.; Zhang, X. Y.; Ren, S. Q.; Sun, J. In *2016 IEEE Conference on Computer Vision and Pattern Recognition (CVPR)* **2016**, 770–778.
- (71) Hu, J.; Shen, L.; Sun, G. In *Proceedings of the IEEE Conference on Computer Vision and Pattern Recognition (CVPR)*, 2018; pp 7132–7141.
- (72) Ronneberger, O.; Fischer, P.; Brox, T. *Medical Image Computing and Computer-Assisted Intervention* **2015**, *9351*, 234–241.
- (73) Goodfellow, I. J.; Pouget-Abadie, J.; Mirza, M.; Xu, B.; Warde-Farley, D.; Ozair, S.; Courville, A.; Bengio, Y. *arXiv* **2014**, 1406.2661.
- (74) Wang, Z.; She, Q.; Ward, T. E. *arXiv* **2019**, 1906.01529.
- (75) Nwankpa, C.; Ijomah, W.; Gachagan, A.; Marshall, S. *arXiv* **2018**, 1811.03378.
- (76) Ioffe, S.; Szegedy, C. *arXiv* **2015**, 1502.03167.
- (77) Smith, J. T.; Yao, R.; Sinsuephon, N.; Rudkouskaya, A.; Un, N.; Mazurkiewicz, J.; Barroso, M.; Yan, P.; Intes, X. *Proc. Natl. Acad. Sci. U. S. A.* **2019**, *116*, 24019–24030.
- (78) Bai, C.; Liu, C.; Yu, X.; Peng, T.; Min, J.; Yan, S.; Dan, D.; Yao, B. *IEEE Photonics Technol. Lett.* **2019**, *31*, 1803–1806.
- (79) Yao, R.; Ochoa, M.; Yan, P.; Intes, X. *Light: Sci. Appl.* **2019**, *8*, 26.
- (80) Li, D.; Chen, C.; Li, J.; Yan, Q. *J. Opt.* **2020**, *22*, 045602.
- (81) Chen, X.; Xie, L.; He, Y.; Guan, T.; Zhou, X.; Wang, B.; Feng, G.; Yu, H.; Ji, Y. *Analyst* **2019**, *144*, 4312–4319.
- (82) Weigert, M.; Schmidt, U.; Boothe, T.; Muller, A.; Dibrov, A.; Jain, A.; Wilhelm, B.; Schmidt, D.; Broaddus, C.; Culley, S.; Rocha-Martins, M.; Segovia-Miranda, F.; Norden, C.; Henriques, R.; Zerial,

- M.; Solimena, M.; Rink, J.; Tomancak, P.; Royer, L.; Jug, F.; Myers, E. W. *Nat. Methods* **2018**, *15*, 1090–1097.
- (83) Ouyang, W.; Aristov, A.; Lelek, M.; Hao, X.; Zimmer, C. *Nat. Biotechnol.* **2018**, *36*, 460–468.
- (84) Nguyen, T. C.; Nehmetallah, G.; Tian, L. *Proc. SPIE* **2019**, *10990*, 1099007.
- (85) Manifold, B.; Thomas, E.; Francis, A. T.; Hill, A. H.; Fu, D. *Biomed. Opt. Express* **2019**, *10*, 3860–3874.
- (86) Lin, H.; Deng, F.; Zhang, C.; Zong, C.; Cheng, J.-X. *Proc. SPIE* **2019**, *10882*, 10882B.
- (87) Wu, Y.; Rivenson, Y.; Wang, H.; Luo, Y.; Ben-David, E.; Bentolila, L. A.; Pritz, C.; Ozcan, A. *Nat. Methods* **2019**, *16*, 1323–1331.
- (88) Zhou, H.; Cai, R.; Quan, T.; Liu, S.; Li, S.; Huang, Q.; Erturk, A.; Zeng, S. *Opt. Lett.* **2020**, *45*, 1695–1698.
- (89) Zhang, H.; Fang, C.; Xie, X.; Yang, Y.; Mei, W.; Jin, D.; Fei, P. *Biomed. Opt. Express* **2019**, *10*, 1044–1063.
- (90) Wu, Y.; Luo, Y.; Chaudhari, G.; Rivenson, Y.; Calis, A.; de Haan, K.; Ozcan, A. *Light: Sci. Appl.* **2019**, *8*, 25.
- (91) Wang, H.; Rivenson, Y.; Jin, Y.; Wei, Z.; Gao, R.; Gunaydin, H.; Bentolila, L. A.; Kural, C.; Ozcan, A. *Nat. Methods* **2019**, *16*, 103–110.
- (92) Li, Y.; Xu, F.; Zhang, F.; Xu, P.; Zhang, M.; Fan, M.; Li, L.; Gao, X.; Han, R. *Bioinformatics* **2018**, *34*, No. i284.
- (93) Halupka, K. J.; Antony, B. J.; Lee, M. H.; Lucy, K. A.; Rai, R. S.; Ishikawa, H.; Wollstein, G.; Schuman, J. S.; Garnavi, R. *Biomed. Opt. Express* **2018**, *9*, 6205–6221.
- (94) Nehme, E.; Weiss, L. E.; Michaeli, T.; Shechtman, Y. *Optica* **2018**, *5*, 458–464.
- (95) Zhao, X.; Wu, Y.; Song, G.; Li, Z.; Zhang, Y.; Fan, Y. *Med. Image Anal.* **2018**, *43*, 98–111.
- (96) Todorov, M. I.; Paetzold, J. C.; Schoppe, O.; Tetteh, G.; Shit, S.; Efremov, V.; Todorov-Volgyi, K.; During, M.; Dichgans, M.; Piraud, M.; Menze, B.; Erturk, A. *Nat. Methods* **2020**, *17*, 442–449.
- (97) Pardo, E.; Morgado, J. M. T.; Malpica, N. *Cytometry, Part A* **2018**, *93*, 620–627.
- (98) Lotfollahi, M.; Berisha, S.; Daeinejad, D.; Mayerich, D. *Appl. Spectrosc.* **2019**, *73*, 556–564.
- (99) Berisha, S.; Lotfollahi, M.; Jahanipour, J.; Gurcan, I.; Walsh, M.; Bhargava, R.; Van Nguyen, H.; Mayerich, D. *Analyst* **2019**, *144*, 1642–1653.
- (100) Hollon, T. C.; Pandian, B.; Adapa, A. R.; Urias, E.; Save, A. V.; Khalsa, S. S. S.; Eichberg, D. G.; D'Amico, R. S.; Farooq, Z. U.; Lewis, S.; Petridis, P. D.; Marie, T.; Shah, A. H.; Garton, H. J. L.; Maher, C. O.; Heth, J. A.; McKean, E. L.; Sullivan, S. E.; Hervey-Jumper, S. L.; Patil, P. G.; Thompson, B. G.; Sagher, O.; McKhann, G. M., 2nd; Komotar, R. J.; Ivan, M. E.; Snuderl, M.; Otten, M. L.; Johnson, T. D.; Sisti, M. B.; Bruce, J. N.; Muraszko, K. M.; Trautman, J.; Freudiger, C. W.; Canoll, P.; Lee, H.; Camelo-Piragua, S.; Orringer, D. A. *Nat. Med.* **2020**, *26*, 52–58.
- (101) Zhang, L.; Wu, Y.; Zheng, B.; Su, L.; Chen, Y.; Ma, S.; Hu, Q.; Zou, X.; Yao, L.; Yang, Y.; Chen, L.; Mao, Y.; Chen, Y.; Ji, M. *Theranostics* **2019**, *9*, 2541–2554.
- (102) Yuan, P.; Rezvan, A.; Li, X.; Varadarajan, N.; Van Nguyen, H. *J. Clin. Med.* **2019**, *8*, 1159.
- (103) Hollon, T. C.; Orringer, D. A. *Mol. Cell Oncol.* **2020**, *7*, 1736742.
- (104) Nadarajan, G.; Hope, T.; Wang, D.; Cheung, A.; Ginty, F.; Yaffe, M. J.; Doyle, S.; Tomaszewski, J. E.; Ward, A. D. *Proc. SPIE* **2019**, *10956*, 109560J.
- (105) Zhang, K.; Zhang, H.; Zhou, H.; Crookes, D.; Li, L.; Shao, Y.; Liu, D. *Comput. Intell. Neurosci.* **2019**, *2019*, 8214975.
- (106) Wang, W.; Taft, D. A.; Chen, Y. J.; Zhang, J.; Wallace, C. T.; Xu, M.; Watkins, S. C.; Xing, J. *Comput. Biol. Med.* **2019**, *108*, 133–141.
- (107) Shen, J.; Li, T.; Hu, C.; He, H.; Liu, J. *Proc. SPIE* **2019**, *10950*, 109502T.
- (108) Lee, J.; Kim, H.; Cho, H.; Jo, Y.; Song, Y.; Ahn, D.; Lee, K.; Park, Y.; Ye, S.-J. *IEEE Access* **2019**, *7*, 83449–83460.
- (109) Fu, C.; Lee, S.; Ho, D. J.; Han, S.; Salama, P.; Dunn, K. W.; Delp, E. J. In *2018 IEEE/CVF Conference on Computer Vision and Pattern Recognition (CVPR) Workshops*, 2018; pp 2302–2308.
- (110) Dunn, K. W.; Fu, C.; Ho, D. J.; Lee, S.; Han, S.; Salama, P.; Delp, E. J. *Sci. Rep.* **2019**, *9*, 18295.
- (111) Rivenson, Y.; Wang, H.; Wei, Z.; de Haan, K.; Zhang, Y.; Wu, Y.; Gunaydin, H.; Zuckerman, J. E.; Chong, T.; Sisk, A. E.; Westbrook, L. M.; Wallace, W. D.; Ozcan, A. *Nat. Biomed. Eng.* **2019**, *3*, 466–477.
- (112) Rivenson, Y.; Liu, T.; Wei, Z.; Zhang, Y.; de Haan, K.; Ozcan, A. *Light: Sci. Appl.* **2019**, *8*, 23.
- (113) Raza, S. E. A.; Cheung, L.; Shaban, M.; Graham, S.; Epstein, D.; Pelengaris, S.; Khan, M.; Rajpoot, N. M. *Med. Image Anal.* **2019**, *52*, 160–173.
- (114) Yan, H.; Yu, M.; Xia, J.; Zhu, L.; Zhang, T.; Zhu, Z. *Vib. Spectrosc.* **2019**, *103*, 102938.
- (115) Weng, S.; Xu, X.; Li, J.; Wong, S. T. C. *J. Biomed. Opt.* **2017**, *22*, 1–10.
- (116) Van Valen, D. A.; Kudo, T.; Lane, K. M.; Macklin, D. N.; Quach, N. T.; DeFelice, M. M.; Maayan, I.; Tanouchi, Y.; Ashley, E. A.; Covert, M. W. *PLoS Comput. Biol.* **2016**, *12*, No. e1005177.
- (117) Thrift, W. J.; Ragan, R. *Anal. Chem.* **2019**, *91*, 13337–13342.
- (118) Shi, H.; Wang, H.; Meng, X.; Chen, R.; Zhang, Y.; Su, Y.; He, Y. *Anal. Chem.* **2018**, *90*, 14216–14221.
- (119) Rodner, E.; Bocklitz, T.; von Eggeling, F.; Ernst, G.; Chernavskaya, O.; Popp, J.; Denzler, J.; Guntinas-Lichius, O. *Head Neck* **2018**, *41*, 116–121.
- (120) Qiu, Z.; Chen, J.; Zhao, Y.; Zhu, S.; He, Y.; Zhang, C. *Appl. Sci.* **2018**, *8*, 212.
- (121) Niioka, H.; Asatani, S.; Yoshimura, A.; Ohigashi, H.; Tagawa, S.; Miyake, J. *Hum. Cell* **2018**, *31*, 87–93.
- (122) Long, F. *J. Med. Imaging (Bellingham)* **2018**, *5*, 036001.
- (123) Liu, J.; Osadchy, M.; Ashton, L.; Foster, M.; Solomon, C. J.; Gibson, S. J. *Analyst* **2017**, *142*, 4067–4074.
- (124) Krauss, S. D.; Roy, R.; Yosef, H. K.; Lechtonen, T.; El-Mashtoly, S. F.; Gerwert, K.; Mosig, A. *J. Biophotonics* **2018**, *11*, No. e201800022.
- (125) Joung, H. A.; Ballard, Z. S.; Wu, J.; Tseng, D. K.; Teshome, H.; Zhang, L.; Horn, E. J.; Arnaboldi, P. M.; Dattwyler, R. J.; Garner, O. B.; Di Carlo, D.; Ozcan, A. *ACS Nano* **2020**, *14*, 229–240.
- (126) Halicek, M.; Dormer, J. D.; Little, J. V.; Chen, A. Y.; Fei, B. *Biomed. Opt. Express* **2020**, *11*, 1383–1400.
- (127) Fan, X.; Ming, W.; Zeng, H.; Zhang, Z.; Lu, H. *Analyst* **2019**, *144*, 1789–1798.
- (128) Chen, C. L.; Mahjoubfar, A.; Tai, L. C.; Blaby, I. K.; Huang, A.; Niazi, K. R.; Jalali, B. *Sci. Rep.* **2016**, *6*, 21471.
- (129) Aljakouch, K.; Hilal, Z.; Daho, I.; Schuler, M.; Krauss, S. D.; Yosef, H. K.; Dierks, J.; Mosig, A.; Gerwert, K.; El-Mashtoly, S. F. *Anal. Chem.* **2019**, *91*, 13900–13906.
- (130) Ho, C. S.; Jean, N.; Hogan, C. A.; Blackmon, L.; Jeffrey, S. S.; Holodniy, M.; Banaei, N.; Saleh, A. A. E.; Ermon, S.; Dionne, J. *Nat. Commun.* **2019**, *10*, 4927.
- (131) Ali, N.; Quansah, E.; Köhler, K.; Meyer, T.; Schmitt, M.; Popp, J.; Niendorf, A.; Bocklitz, T. *Translational Biophotonics* **2019**, *1*, No. e20190003.
- (132) Rauf, A. P.; Butke, J.; Kupper, C.; Grosserueschkamp, F.; Gerwert, K.; Mosig, A. *Bioinformatics* **2020**, *36*, 287–294.
- (133) Zhang, L.; Schaeffer, H. *J. Math. Imaging Vis.* **2020**, *62*, 328–351.
- (134) He, H.; Xu, M.; Zong, C.; Zheng, P.; Luo, L.; Wang, L.; Ren, B. *Anal. Chem.* **2019**, *91*, 7070–7077.
- (135) Zhang, J.; Zhao, J.; Lin, H.; Tan, Y.; Cheng, J. X. *J. Phys. Chem. Lett.* **2020**, *11*, 8573–8578.
- (136) Meijering, E. *IEEE Signal Proc. Mag.* **2012**, *29*, 140–145.
- (137) Kostrykin, L.; Schnorr, C.; Rohr, K. *Med. Image Anal.* **2019**, *58*, 101536.
- (138) Trajanovski, S.; Shan, C.; Weijtmans, P. J. C.; Brouwer de Koning, S. G.; Ruers, T. J. M. *IEEE Trans. Biomed. Eng.* **2020**.

- (139) Zhang, Y.; de Haan, K.; Rivenson, Y.; Li, J.; Delis, A.; Ozcan, A. *Light: Sci. Appl.* **2020**, *9*, 78.
- (140) Albrecht, T.; Slabaugh, G.; Alonso, E.; Al-Arif, S. *Nano-technology* **2017**, *28*, 423001.
- (141) Xu, J. C.; Qin, G. G.; Luo, F.; Wang, L. N.; Zhao, R.; Li, N.; Yuan, J. H.; Fang, X. H. *J. Am. Chem. Soc.* **2019**, *141*, 6976–6985.
- (142) Shin, H.; Oh, S.; Hong, S.; Kang, M.; Kang, D.; Ji, Y.-g.; Choi, B. H.; Kang, K.-W.; Jeong, H.; Park, Y.; Hong, S.; Kim, H. K.; Choi, Y. *ACS Nano* **2020**, *14*, 5435–5444.
- (143) Lu, W. L.; Chen, X. Q.; Wang, L.; Li, H. F.; Fu, Y. V. *Anal. Chem.* **2020**, *92*, 6288–6296.
- (144) Rivenson, Y.; Wu, Y.; Ozcan, A. *Light: Sci. Appl.* **2019**, *8*, 85.
- (145) Gidaris, S.; Bursuc, A.; Komodakis, N.; Perez, P.; Cord, M. In *Proceedings of the IEEE/CVF International Conference on Computer Vision (ICCV)*, 2019; pp 8059–8068.
- (146) Sun, Q.; Liu, Y.; Chua, T.-S.; Schiele, B. *Proceedings of the IEEE/CVF Conference on Computer Vision and Pattern Recognition (CVPR)*, 2019; pp 403–412.
- (147) Lake, B. M.; Salakhutdinov, R.; Tenenbaum, J. B. *Science* **2015**, *350*, 1332–1338.
- (148) Baldi, P. *Annu. Rev. Biomed. Data Sci.* **2018**, *1*, 181–205.
- (149) Selvaraju, R. R.; Cogswell, M.; Das, A.; Vedantam, R.; Parikh, D.; Batra, D. In *Proceedings of the IEEE International Conference on Computer Vision (ICCV)*, 2017; pp 618–626.
- (150) Zhang, J.; Bargal, S. A.; Lin, Z.; Brandt, J.; Shen, X.; Sclaroff, S. *Int. J. Comput. Vision* **2018**, *126*, 1084–1102.
- (151) Hinton, G. E.; Salakhutdinov, R. R. *Science* **2006**, *313*, 504–507.
- (152) Hurtik, P.; Molek, V.; Perfilieva, I. *Pattern Recogn.* **2020**, *103*, 107291.
- (153) He, K.; Fan, H.; Wu, Y.; Xie, S.; Girshick, R. In *Proceedings of the IEEE/CVF Conference on Computer Vision and Pattern Recognition (CVPR)*, 2020; pp 9729–9738.